Tuning the thermal activation atmosphere breaks the activity-stability trade-off of Fe-N-C oxygen reduction fuel cell catalysts

Yachao Zeng^{1,12}, Chenzhao Li^{2,12}, Boyang Li^{3,12}, Jiashun Liang^{1,12}, Michael J. Zachman⁴, David A. Cullen⁴, Raphael P. Hermann⁵, E. Ercan Alp⁶, Barbara Lavina^{6,7}, Stavros Karakalos⁸, Marcos Lucero⁹, Bingzhang Zhang¹, Maoyu Wang⁹, Zhenxing Feng⁹, Guofeng Wang^{3,*}, Jian Xie^{2,*}, Deborah J. Myers^{10,*}, Jean-Pol Dodelet¹¹, and Gang Wu^{1,*}

¹ Department of Chemical and Biological Engineering, University at Buffalo, The State University of New York, Buffalo, New York 14260, USA. Email: gangwu@buffalo.edu

² Department of Mechanical and Energy Engineering, Purdue School of Engineering and Technology, Indiana University-Purdue University, Indianapolis, Indiana 46202, USA. Email: jianxie@iupui.edu

³ Department of Mechanical Engineering and Materials Science, University of Pittsburgh, Pittsburgh, Pennsylvania 15260, USA. Email: guw8@pitt.edu

⁴ Center for Nanophase Materials Sciences, Oak Ridge National Laboratory, Oak Ridge, Tennessee 37831, USA.

⁵ Materials Science and Technology Division, Oak Ridge National Laboratory, Oak Ridge, Tennessee 37831, USA.

⁶ Advanced Photon Source, Argonne National Laboratory, Lemont, Illinois 60439, USA

⁷Center for Advanced Radiation Sources, The University of Chicago, Chicago, IL 60637, USA

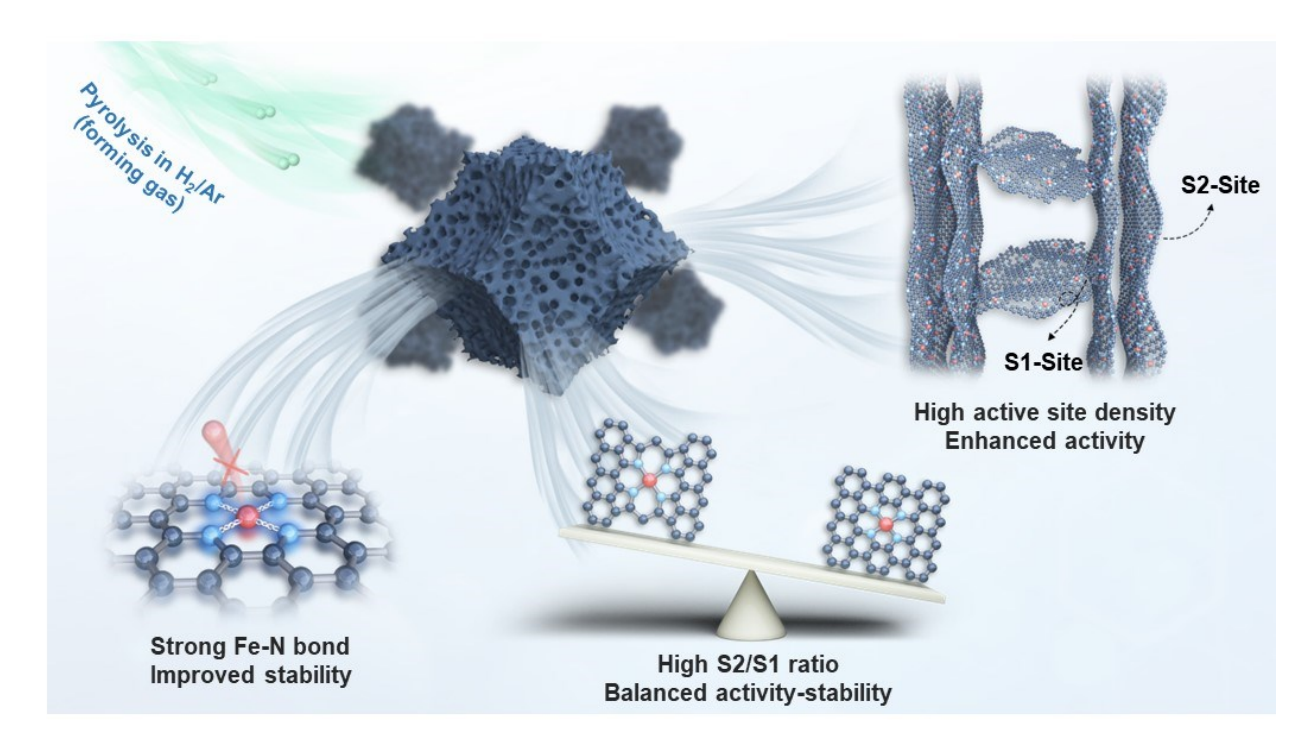
⁸ Department of Chemical Engineering, University of South Carolina, Columbia, South Carolina 29208, USA.

⁹ School of Chemical, Biological, and Environmental Engineering Oregon State University, Corvallis, Oregon 97331, USA

¹⁰ Chemical Sciences and Engineering Division, Argonne National Laboratory, Lemont, Illinois 60439, USA. Email: dmyers@anl.gov

¹¹ INRS-Énergie, Matériaux et Télécommunications, 1650 Boulevard Lionel Boulet, Varennes, Québec J3X 1P7, Canada

¹² These authors contribute equally.



Abstract. Fe-N-C catalysts are the most promising platinum group metal (PGM)-free oxygen-reduction catalysts but suffer from a low density of active metal sites and the activity-stability trade-off. Here we report a Fe-N-C catalyst prepared by adding optimal H₂ to the traditional inert atmosphere during the thermal activation. The presence of H₂ significantly increases the total density of pyrrolic- (S1) and pyridinic-N coordinated FeN₄ (S2) sites, suppressing unstable S1 sites and favoring the stable S2 sites with shortened Fe-N bond lengths. We proposed that the intrinsically stable S2 sites are likely in well-graphitized carbon layers, while S1 sites exist in less-graphitized carbon. H₂ could remove unstable S1 sites and retain stable S2 sites during the pyrolysis to break the challenging activity-stability trade-off. The Fe-N-C catalyst in membrane electrode assemblies maintained a current density of 67 mA cm⁻² at 0.8 V (H₂-air) after 30,000 voltage cycles (0.60 to 0.95 V under H₂/air), achieving encouraging durability and performance simultaneously.

Introduction

The development of platinum-group-metal (PGM)-free catalysts significantly benefits the cost reduction of hydrogen proton-exchange membrane fuel cells (PEMFCs) for sustainable large-scale applications^{1,2}. The atomically-dispersed and nitrogen-coordinated FeN₄ sites hosted in carbon (Fe-N-C) are the most promising catalysts for replacing Pt for the cathodic oxygen reduction reaction (ORR) in the challenging acidic environment of the PEMFC³⁻⁸. However, over the past several decades, performance and durability improvements of Fe-N-C catalysts are still significantly limited due to the insufficient understanding of active sites, low site density, poor stability, and an activity-stability trade-off⁹.

Like Pt active sites, the adsorption strength of O₂ and ORR intermediates on FeN₄ active sites is too strong^{10,11}. The activation barrier to cleave the O-O bond is too high for the preferred 4e⁻ transfer pathway. In addition, achieving comparable or even better stability to current Pt catalysts remains a significant challenge, primarily due to the possible demetallation *via* Fe-N bond breaking during the ORR¹². Regulating the electronic and geometric structures of FeN₄ active sites to modulate adsorption energies, reduce activation energies, and strengthen Fe-N bonds is critical for improving the intrinsic activity and stability of FeN₄ sites^{13,14}.

One of the recent breakthroughs is the identification of two types of FeN₄ sites in Fe-N-C catalysts based on *in-situ* Mössbauer and *operando* X-ray absorption spectroscopy experiments¹⁵. An FeN₄C₁₂ moiety contains pyrrolic N ligations, often denoted as the S1 site. The other FeN₄C₁₀ moiety with pyridinic N environments is denoted as the S2 site¹⁵. S1 sites are more intrinsically active but irreversibly and rapidly degraded to inactive ferric oxides during the ORR, causing dramatic activity loss. S2 sites are more stable against demetallation but less active due to stronger adsorption of oxygen and intermediates⁶. Therefore, it is highly desirable to synthesize a catalyst

containing significantly increased densities of S1 and S2 sites with enhanced intrinsic activity and stability simultaneously. However, achieving this goal using traditional synthesis approaches is nearly impossible based on previously reported catalysts in literature ^{16,17}.

Herein, we found that local carbon and nitrogen coordination structures of FeN₄ sites and their site density could be regulated by adding H₂ to a traditional inert Ar atmosphere (i.e., forming gas) for thermal activation, a critical step to creating active sites during the catalyst synthesis. Significantly, due to the accelerated carbon gasification process in the presence of H₂ at high temperatures, forming gas could favor the retention of stable S2 sites in well-graphitized carbon and remove the unstable S1 sites in amorphous carbon in catalysts. Unlike previously identified FeN₄ sites, the S1 and S2 sites contain shortened Fe-N bonds due to the hydrogenation of carbon atoms adjacent to the FeN₄ moieties during the thermal activation under the forming gas, which is theoretically predicted to yield enhanced intrinsic stability while maintaining high activity. The resulting Fe-N-C catalyst thus leads to exceptional activity and improved stability. A membrane electrode assembly (MEA) made from the Fe-N-C cathode reaches 50.8 mA cm⁻² at 0.9 V_{iR-free} under 1.0 bar O₂, exceeding the U.S. DOE 2025 target (44 mA cm⁻²). Under practical 1.0 bar air, the MEA generated current densities of 191.0 and 745.4 mA cm⁻² at 0.80 and 0.67 V, respectively, which outperforms a typical Pt/C cathode (TEC10V20E, 0.1 mg_{Pt} cm⁻²) in the kinetic voltage region (>0.75 V). Due to the enhanced intrinsic stability of both S1 and S2-typed FeN₄ sites, MEA performance degradation is significantly mitigated, capable of retaining 67 mA cm⁻² at 0.8 V after 30,000 cycles voltage AST under H₂/air conditions. The knowledge obtained from experimental and theoretical results in this work elucidates that the formation process of FeN₄ sites and their local coordination structures can be regulated by tuning the atmosphere during thermal activation. This is essential to break the activity-stability trade-off barrier and design viable Fe-N-C catalysts

with adequate performance and durability for PEMFCs.

Results

Catalyst synthesis, activity, and stability

Pyrolyzing precursors under an inert atmosphere (*e.g.*, N₂ or Ar) has long been the prevailing approach for forming FeN₄ active sites in Fe-N-C catalysts¹⁸⁻²⁰. Dodelet and Kramm *et al.* found that treatment in NH₃/N₂ following this pyrolysis step can efficiently enhance ORR activity due to the formation of substantial micropores to host increased numbers of active sites²¹⁻²⁴. In principle, NH₃ could be further decomposed into H₂ and N₂ at the elevated temperature of up to 900 °C during the catalyst synthesis²⁵. We hypothesized that, besides the benefits of directly using NH₃, the optimal H₂ content combined with controlled heating temperatures and duration may play a role in tuning active site structures and locations. Here, we uncover that optimization of the H₂ content in forming gas (FG) (*i.e.*, H₂/Ar mixture) can efficiently enhance ORR activity and stability by simultaneously increasing metal site density, modifying carbon morphologies and structures, and regulating the Fe-N bond length as illuminated in **Figure 1a**.

During the catalyst synthesis, Fe₂O₃-enclosed ZIF-8 nanocrystals were used as a precursor due to the effectiveness of forming atomically dispersed single iron sites with increased density⁶. When the H₂ content in the forming gas was increased from 0 (*i.e.*, Ar atmosphere) to 2 mol.% (denoted as Fe-N-C-2%FG), the ORR activity of the catalyst in 0.5 M H₂SO₄ electrolyte was greatly promoted (**Figure 1b**), evidenced by an increase of half-wave-potential ($E_{1/2}$) from 0.84 to 0.88 V vs. RHE under established testing conditions (600 µg cm⁻², 25 °C, and 900 r.p.m.). When the H₂ content was increased to 5 mol. %, the catalyst exhibited an $E_{1/2}$ up to 0.92 V, outperforming

a baseline Pt/C catalyst at a standard loading of 60 μg_{Pt} cm⁻² in an acidic electrolyte (0.1 M HClO₄). Further increasing H₂ content to 10 mol.% only led to a minor improvement in ORR activity, achieving an $E_{1/2}$ of 0.93 V with better reproducibility (Supplementary Figure 1). Reductive pyrolysis atmospheres were explored in the preparation of Fe-N-C catalysts^{23,24,26,27}. A combination of the ZIF-8/Fe₂O₃ precursors, optimal H₂ content, and favorable thermal conditions is crucial for producing active Fe-N-C catalysts in this work (Supplementary Table 1). We comprehensively studied various synthetic parameters, including the Fe content and heating procedures, which are crucial for achieving high activity (Supplementary Figure 2). Also, the yield of Fe-N-C catalysts was decreased with an increase of H₂ concentration during the pyrolysis atmosphere, likely due to the effective removal of less-graphitized carbon and residual zinc with increased porosity, a key to hosting stable FeN₄ active sites with increased density in catalysts (Supplementary Figure 3 and Supplementary Table 2). We determined that the active site density (SD), as calculated using electrochemical stripping of nitrite^{28,29}, increased with higher H₂ content in the pyrolysis atmosphere (Figure 1c and Supplementary Figure 4), suggesting enhanced activity for the ORR.

Different iron precursors, such as Fe ions, were also used to prepare Fe-N-C catalysts to evaluate the universal effectiveness of forming gas for the ORR activity enhancement^{30,31}. As shown in **Supplementary Figure 5a**, the Fe-ion-doped ZIF-8-derived catalyst (denoted as Fe-ion-NC-FG) prepared in the forming gas also exhibited improved ORR activity ($E_{1/2} = 0.896 \text{ V}$) over the catalyst pyrolyzed in traditional Ar ($E_{1/2} = 0.852 \text{ V}$). The possible advantage of using Fe₂O₃ nanoparticles over conventional Fe ions is that H₂ facilitates the decomposition of Fe₂O₃

nanoparticles, generating more single Fe sites and transforming them into FeN₄ sites. The oxygen in Fe₂O₃ may also react with H₂ and generate H₂O, which is favorable for carbon gasification during pyrolysis, a critical process to create porosity and retain stable active sites in carbon. In addition to high activity, the catalysts pyrolyzed in forming gas exhibited enhanced 4e⁻ selectivity (**Supplementary Figure 5b**). A similar tendency to promote activity and selectivity for the Fe-N-C catalysts derived from both ZIF-8/Fe₂O₃ and Fe-ion-doped ZIF-8 precursor further verified the advantages of the forming gas during the catalyst synthesis.

As shown in **Supplementary Figure 6**, there is only Fe^{3+}/Fe^{2+} redox presented in the CV profiles for all studied Fe-N-C catalysts. The potential of Fe^{3+}/Fe^{2+} redox does not change significantly with an increase in the scanning rate, indicating the Fe^{3+}/Fe^{2+} transition has good reversibility. The half-height width of these peaks is ca. 97 mV, very close to the theoretical value of 96 mV expected for a reversible one-electron process involving surface species. Intriguingly, the redox potential of all Fe-N-C catalysts generally ranges from 0.64 to 0.67 V_{RHE} , even though there are notable differences in their ORR activities. Therefore, we considered that the intrinsic ORR activity is not directly associated with Fe^{2+}/Fe^{3+} redox.

The catalytic properties (*i.e.*, activity, 4e⁻-selectivity, and stability) of the Fe-N-C catalysts prepared from different atmospheres as a function of H₂ content were further compared using a rotating ring-disk electrode (RRDE) in O₂-saturated 0.5 M H₂SO₄ solution through recording initial activity and selectivity, followed by standard ASTs (0.60 to 0.95 V for 30,000 potential cycles) to study ORR stability (**Figure 1d** and **Supplementary Figure 7**). The corresponding $E_{1/2}$ and kinetic current density at 0.9 V_{RHE} ($j_k@0.9$ V) were identified as indicators for activity, and

their changes during the AST were used for evaluating stability. Among others, the Fe-N-C-10%FG exhibited the highest activity at the end of the AST, with an $E_{1/2}$ of 0.83 V, close to the initial $E_{1/2}$ of the Fe-N-C-Ar catalyst. Notably, the Fe-N-C-Ar and the Fe-NC-10%FG catalysts presented different degradation modes during the stability ASTs (**Supplementary Figure 7**). The ORR activity of the Fe-N-C-10%FG catalyst stabilized after 5,000 potential cycles, suggesting the existence of active sites with intrinsic stability. In contrast, the Fe-N-C-Ar continuously lost activity up to 30,000 cycles during the AST. The different degradation behaviors imply that the nature of active sites dominating the ORR activity of these two catalysts is not the same, to be discussed in the following characterization sections.

Fuel cell MEA performance and durability

The best-performing Fe-N-C-FG catalyst was further studied in both hydrogen fuel cells and direct methanol fuel cells (DMFCs). When using H₂ at the anode, the MEA with the Fe-NC-10%FG cathode generated 50.8 mA cm⁻² at 0.9 V_{iR-free} under 1.0 bar O₂ (**Figure 2a**). This value was obtained according to the US DOE ElectroCat Consortium's recommended testing protocol³³ and significantly exceeded the 2025 target (44.0 mA cm⁻²). Under practical air conditions (1.0 bar), the same MEA generated 191.0 and 745.0 mA cm⁻² at 0.80 and 0.67 V averaged from three tests, respectively (**Supplementary Figure 8** and Supplementary Table 3). The achieved performance already outperforms all previously reported Fe-N-C catalysts (**Supplementary Figure 9** and **Supplementary Table 4**) and a typical Pt/C cathode (TEC10V20E, 0.1 mg_{Pt} cm⁻²) in the kinetic voltage range (*i.e.*, > 0.75 V, **Figure 2b**). An optimal relative humidity (RH) of 75 % was

determined to mitigate the water flooding within the thick PGM-free cathode (Supplementary Table 5).

A square-wave voltage cycling protocol under H₂/air was employed for ASTs³³ to evaluate catalyst durability under actual fuel cell operating conditions. The performance loss of the Fe-N-C-Ar cathode in an MEA was significant: 90 % at 0.8 V (Figure 2c and Supplementary Table 6). In contrast, the Fe-N-C-10%FG cathode exhibited significantly enhanced durability, retaining 67 mA cm⁻² at 0.8 V after 30,000 voltage cycles, corresponding to a loss of 64.9 % (Figure 2d)³⁴. Although the voltage loss at 0.8 A cm⁻² is still higher than US DOE targets (i.e., 84 mV vs. 30 mV)³⁵ (Supplementary Table 7), the achieved stability enhancement is superior to all reported Fe-N-C catalysts^{1,2}. Like the catalyst degradation in RRDE tests, the Fe-N-C-Ar catalyst decayed continuously during the MEA ASTs. In contrast, the Fe-N-C-10%FG catalyst stabilized after 5,000 AST cycles in H₂-air. Stability ASTs for the Fe-N-C-10%FG catalyst were also performed under an H₂/N₂ atmosphere. They exhibited comparable performance loss to the H₂/air conditions (Supplementary Figure 10 and Supplementary Table 8), suggesting that catalyst degradation associated with the possible demetallation is primarily driven by electrochemical voltage/potential cycling, rather than chemical dissolution or oxidation.

Compared to a Pt/C (TEC10V20E) cathode (0.1 mg_{Pt} cm⁻²), the Fe-N-C-10%FG cathode-based MEA demonstrated similar durability (**Figure 2e**) as significant performance loss was also observed with the Pt/C cathode after identical 30,000-cycle AST. In addition to voltage cycling AST stability evaluation, we also carried out a durability test for these Fe-N-C cathodes by holding them at a constant voltage of 0.67 V for up to 200 hours (**Figure 2f**). Compared with previously

reported highly active Fe-N-C catalyst treated with NH₄Cl (denoted as Fe-AC)⁶, the Fe-N-C-10%FG cathode showed a much higher retention of current density, likely due to the structure change of S1 and S2 sites with simultaneously enhanced intrinsic activity and stability. The observed performance degradation, especially at the initial stage around 50 hours, is likely due to the loss of S1 sites, which are intrinsically unstable during the ORR. As for the Fe-N-C-Ar catalyst, a fast initial decay of around 25 hours was observed due to the rapid demetallation of the S1-type sites, followed by a similar decay rate to that of the Fe-N-C-FG catalyst arising from the more stable S2-type sites. All these experimental results agree well with the demetallation energy calculated, as discussed in the later sections.

Unlike Pt, Fe-N-C catalysts are intrinsically methanol-tolerant³⁶, which is highly desirable for DMFCs to replace traditional Pt cathodes with reduced cost and mitigated Pt poisoning. Thus, the Fe-N-C-10%FG was further studied as a cathode in DMFCs, which exhibited a peak power density of 275 mWcm⁻² at a loading of 3.0 mg_{PGM} cm⁻² at the anode, significantly exceeding a Pt/C cathode (80 mW cm⁻²) under the similar conditions (**Figure 2g**). Like the behavior in H₂ fuel cells, the Fe-N-C-FG cathode decayed after 10,000 voltage cycles and then stabilized up to 30,000 cycles during an AST (0.4 to 0.8 V). Meanwhile, a short-term 20-h steady-state test at 0.5 V verified its promising stability under DMFC conditions (**Figure 2h**), retaining a respectable current density of 250 mA cm⁻².

Catalyst Characterization for Mechanistic Understanding

The developed Fe-N-C-FG catalysts demonstrated encouraging performance and durability in

hydrogen and direct methanol fuel cells. We further carried out extensive characterization to elucidate active sites and relevant mechanisms of performance improvements. First, ⁵⁷Fe Mössbauer spectroscopy, which is highly sensitive to the oxidation state, electron configuration, and atomic coordination environment of Fe nuclei^{34,37,38}, was acquired at both room and low temperature (6.5 K) to reveal the impact of pyrolysis atmosphere on coordinating environments and local structures of FeN₄ sites in catalysts (Figure 3, Supplementary Tables 9 and 10). Generally, the Mössbauer spectra of the Fe-N-C catalysts were mainly fit with two doublets associated with single Fe sites coordinated with nitrogen. In addition, insignificant singlet and sextet peaks were assigned to Fe nanoparticles remaining in the catalysts. In particular, D1 doublets with lower isomer shifts (δ) and quadrupole splitting (QS) values were assigned to the high-spin S1 moiety as discussed before, in which a Fe nucleus coordinates with four porphyrinic (i.e., pyrrolic) nitrogen ligands. The D2 doublets featuring larger QS values were assigned to a low- or intermediate-spin S2 moiety, where the Fe nucleus coordinates with four pyridinic nitrogen ligands. At first, the S1/S2 ratios were decreased from 1.56 for the Fe-N-C-Ar catalyst to 0.92 for the Fe-N-C-10%FG catalyst, indicating that the highly stable S2-type FeN₄ sites become dominant due to forming gas. At room temperature, superparamagnetic Fe-nano-oxides contribute with a doublet signal similar to the D1 signal^{39,40}. To exclude the interference Fe-nano-oxides, low-temperature ⁵⁷Fe Mössbauer spectroscopy was performed at 6.5 K (**Figure 3b** and **Supplementary Table 11**), showing no superparamagnetic Fe-nano-oxides in the Fe-N-C-10%FG catalyst. To quantitatively determine the absolute S1 and S2 sites in various catalysts, the Fe content was determined by ICP-OES (Supplementary Table 12). The Fe content increased from 0.15 wt.% in ⁵⁷Fe-N-C-Ar to 0.73

wt.% in 57 Fe-N-C-10%FG. Notably, the Zn content of the 57 Fe-N-C catalysts decreased to beneath the detection limit when the H_2 percentage was > 2 mol.%. The calculated content of S1 and S2 sites in the Fe-N-C-10%FG is 3.2 times higher than the Fe-N-C-Ar catalysts (**Figures 3c**, **d** and **Supplementary Figure 11**). This is in general agreement with the increase of side density by a factor of 4.3 found by electrochemical measurements (see **Figure 1c**). Therefore, the significantly increased content of S1 and S2 sites and the dominant intrinsically stable S2 sites in the forming gas-treated catalysts contribute to improved activity and stability. Unlike the Ar atmosphere, metallic Fe was detected in forming gas at a lower temperature, which could catalyze the graphitization of the carbon matrix⁴¹, as evidenced by the Raman spectra (**Supplementary Figure 12**).

The morphologies of the Fe-N-C-Ar and the Fe-N-C-10%FG catalysts were compared with respect to particles, carbon structures, and atomic single-site dispersion in the carbon matrix (Figure 4). The Fe-N-C-Ar catalyst presented well-defined polyhedral particles with distinct edges and surfaces (Figure 4a). In contrast, highly curved carbon structures with significant deformation and roughness at the particle surface were apparent in the Fe-N-C-10%FG catalyst (Figure 4e). Supplementary Figure 13 further compared the morphologies of the catalyst prepared in the pyrolysis atmospheres with different H₂ content. Increasing the H₂ concentration of the pyrolysis atmosphere leads to more deformed catalyst particles with concave facets. Unlike the Fe-N-C-Ar catalyst with a homogeneous porosity distribution, hollow structures can often be found in the Fe-N-C-10%FG catalyst (Figure 4f). Both carbon particle surfaces exhibit textured surfaces (Figures 4c, g) with porous interior structures (Figures 4d, h). Fe nanoparticles can also be sporadically

observed in the Fe-N-C-10%FG catalysts, corresponding to a singlet and sextet in the ⁵⁷Fe Mössbauer spectra. These observed Fe nanoparticles were encapsulated within compact, thick carbon shells (up to 14 layers, **Figure 4i**). Some of them can even catalyze the growth of nitrogendoped multiwall carbon nanotubes (MWCNTs, **Figures 4j-k**), hosting atomically dispersed metal sites according to aberration-corrected annular-dark-field scanning transmission electron microscopy (ADF-STEM, **Figure 4l**).

ADF-STEM images were further acquired to elucidate both catalysts at the atomic level (Figures 5a-5d). The edges of the Fe-N-C-10%FG catalyst consisted of "crumpled" few-layer thick graphitic structures, and similar features were observed in the Fe-N-C-Ar. Both Ar- and forming gas-treated catalysts presented atomically dispersed iron sites (Figures 5b, 5d). Consistent with ICP-OES measurements, the STEM-EDS quantification indicated that the Fe-N-C-FG catalyst had significantly reduced Zn content relative to the Fe-N-C-Ar catalyst (Supplementary **Table 13**). Brunauer-Emmett-Teller (BET) and pore analyses were performed to assess the impact of the pyrolysis atmosphere on catalyst porosities, as microporosity is crucial to hosting active sites 12,46 and mesoporosity could facilitate O₂ transport and improve ionomer distribution in catalyst layers (Figure 5e)^{47,48}. BET surface areas were increased from 824.4 for the Fe-N-C-Ar to 1187.3 m² g⁻¹ for the Fe-N-C-10%FG (Supplementary Figure 14 and Supplementary Table 14), corresponding to significantly increased micropore surface area from 753.0 to 1047.0 m² g⁻¹. Notably, external surface areas, composed of meso- and macro-porosity, increased monotonically with H₂ concentration, likely due to the graphitic carbon shells formed in the forming gas causing thermal stress and uneven shrinkage of carbon particles^{49,50}. The presence of graphitic carbon

shells and carbon nanotubes was evidenced by the appearance of a 2D peak of the Raman spectrum of the Fe-N-C-10%FG catalyst (**Figure 5f and Supplementary Figure 12**) along with STEM images, which relates to the stack of multilayered graphitic structures in the catalyst⁵¹. In contrast, there was no 2D peak in Raman spectra until the H₂ concentration was above 2%, indicating a less graphitized carbon structure from the H₂-deficient pyrolysis atmosphere. Notably, the resulting concaved surfaces contributed to the high specific surface area⁵², and the increased fraction of graphitic structures could benefit stability improvement of the Fe-N-C-FG catalyst⁵³.

X-ray absorption near-edge spectroscopy (XANES) analysis indicated that the absorption edge energies of both Fe-N-C catalysts were located between those of Fe(II) and Fe(III) references, FeO/Fe(II)pc and Fe₂O₃, respectively (**Figure 5g**), suggesting that the valence state is between 2+ and 3+42,43. Furthermore, the Fe-N-C-10%FG catalyst exhibited slightly lower edge energy than the Fe-N-C-Ar, likely due to the presence of trace Fe metal, which is also evident in the Fourier transform of the extended X-ray absorption fine structure (FT-EXAFS) data (Figure 5h). Notably, the Fourier transforms of both catalysts indicate the presence of a scattering path at similar radial distances as that for the Fe(II)Pc standard, indicating that the catalysts contain a similar pyrrolic N coordination environment. The best-fitting result indicated a coordination number (C/N) of 4.0 (± 1) in the first shell of Fe species in these Fe-N-C catalysts (Supplementary Table 15)⁴⁴. The electronic state of the Fe-N-C catalyst will usually change during the MEA preparation. ⁴⁵ To study the electronic state of Fe in the prepared electrode, we prepared a Fe-N-C-10%FG electrode with an identical ink recipe for MEA studies. XAS with high resolution was recorded and fitted to compare the electronic state of Fe in the electrode and catalyst (Figure 5g). The XANES line shape

for all samples looks similar to Fe(II)Pc. The prepared electrode (Fe-10%FG-Electrode) and the catalyst powder (Fe-10%FG-Catalyst) have a similar pre-edge and rising edge energy positions revealing similar electronic structure. The white line intensity in the electrode was slightly increased. However, EXAFS reveals similar local structure environments for the samples. The exact nature of the bonded ligands is difficult to distinguish, even in high-quality data⁴⁵. It concludes that the electrode preparation process did not change the oxidation state and local coordination. Extended X-ray absorption fine structure (EXAFS) fitting suggested a decreased Fe-N bond length was induced by the forming gas pyrolysis atmosphere, from 2.02 Å in the Fe-N-C-Ar catalyst to 1.95 Å in the Fe-N-C-10%FG catalyst (**Figure 5h**). The shortened Fe-N bond of the Fe-N-C-10%FG catalyst is likely the origin of the enhanced stability measured by RDE and MEAs, which is further elucidated in the following theory section.

Discussion on the promotional role of H₂ and the possible S1 and S2 site locations.

Based on the ADF-STEM images, the ZIF-8-derived Fe-N-C catalysts often contain multilayer graphene domains (Figures 5b, 5d, and **Supplementary Figure 15**). The inter-layer spacing of the carbon sheets has a relatively broad distribution of d-spacings (between 0.35 and 0.41 nm), similar to what has been measured for furnace turbostratic carbon black grades⁵⁴. Between these multilayers lies a complex network of mesopores up to ~20 nm with surfaces consisting of defective N-doped carbon layers. Single Fe sites are represented by white dots in ADF-STEM images throughout the support, including multiple carbon layers and less-graphitized carbon.

When the thermal atmosphere was changed from Ar to forming gas, the presence of H₂ multiplies the gasification of carbon structures (**Supplementary Note 1**). The carbon layers with

less graphitization react faster than the more graphitized ones. Therefore, more mesopore volume results from the pyrolysis in the presence of H₂, and the mesopore volume is increased when more H₂ is added to Ar up to 10% H₂, for which it saturates at about 270% relative to the mesopore volume at 0%H₂ (*i.e.*, Ar). Usually, FeN₄ sites need carbon support to carry out the ORR in the catalysts. The catalytic sites disappear if the carbon support is removed due to gasification. Therefore, upon adding H₂ during the pyrolysis, Fe sites located on the mesoporous surfaces of the carbon could be decreased due to carbon gasification. In contrast, those in the multiple graphene layers are less likely to be lost.

The Mössbauer spectroscopy analyses enable us to identify the specific structures of FeN₄ sites in catalysts. We postulate that the S1-type FeN₄ site, where the four nitrogen atoms are of the pyrrolic type, is hosted on the microporous surfaces of the less graphitized carbon because it is challenging to integrate into a graphitic structure. The S2-type FeN₄ site, where the four nitrogen atoms are pyridinic, can easily be integrated into a graphitic structure, such as the multilayer turbostratic regions. The drastic increase of the mesoporosity upon introducing 10% H₂ in Ar (*i.e.*, forming gas) and the percentages of S1 and S2 of the Fe-species in Mössbauer spectra (both the room and low temperatures) of the catalysts can be well linked following: (i) the relative decrease of the fraction of S1 sites in **Supplementary Figures 11b and 11e** when 10% H₂ is introduced in Ar during the synthesis of the Fe-N-C-FG catalyst is due to the enhanced gasification of carbon structures in H₂ to remove less-graphitized carbon-containing S1 sites; (ii) there is practically no change in the absolute content of S2 in the same figures upon introduction of 10% H₂. Therefore, we conclude that S1-type sites are predominantly hosted in the less-graphitized carbon layers of

the carbon support mesopores, whereas S2-type sites are mainly found in the more-graphitized multiple graphene layers of the same supports, which is in good agreement with the structure of the two sites and their relative stability in fuel cells.

Theoretical elucidation via DFT calculations

We further performed the first principles density functional theory (DFT) calculations to understand the influence of thermal activation atmosphere on the activity and stability of S1 and S2-typed FeN₄ sites embedded in carbon. Considering that the forming gas environment used in our synthesis process could introduce additional hydrogen bonded with carbon, we constructed two S1-4H and S2-4H types of sites with four hydrogen atoms bonded with the carbon atoms immediately adjacent to the FeN₄ moieties (**Figure 6a, Supplementary Note 2** and **Supplementary Figure 16**).

First, we compared the formation enthalpy of the S1 and S2 type FeN₄ moieties with and without hydrogen bonded to carbon to estimate the formation possibility of FeN₄ sites under different atmosphere environments (forming gas *vs.* Ar). As shown in **Figure 6b**, **Supplementary Figures**17a and 17b, we predicted that the formation enthalpy of S1-4H was 0.27 eV lower than S1 and the formation enthalpy of S2-4H was 0.59 eV lower than S2. A lower formation enthalpy would lead to a higher formation possibility of FeN₄ sites. Thus, adding hydrogen could enhance the formation possibility of both S1 and S2 type FeN₄ sites embedded in carbon, thus explaining why the Fe-N-C-FG catalyst contained much higher S1 and S2 sites than the Fe-N-C-Ar catalyst.

Moreover, we calculated the enthalpy change for the transition of a single Fe site from the S2

type to the S1 type N₄ moiety under different atmosphere environments. As shown in **Figure 6b**, **Supplementary Figures 17c** and **17d**, we predicted that this enthalpy change would increase from 0.34 to 0.66 eV if a single Fe atom is converted from S2 to S1 sites when the carbon atoms immediately adjacent to the FeN₄ moiety were hydrogenated. Hence, introducing hydrogen is predicted to favor the formation of the S2 site relative to S1 site with an increased energy barrier from S2 to S1 transition, explaining the higher S2/S1 ratio in the Fe-N-C-FG catalyst than the Fe-N-C-Ar catalyst.

Furthermore, electronic structure analysis was conducted to evaluate the charge transfer between FeN₄ moiety and carbon matrix. The charge density difference plot (**Figure 6c**) showed electron accumulation near the FeN₄ sites with hydrogen bonded to carbon. The Bader charge analysis⁵⁵ quantitatively showed that such electron accumulation was 0.18e on the S1 type FeN₄ site and 0.37e on the S2 type FeN₄ site. This prediction indicates that introducing hydrogen near FeN₄ sites could enhance the interaction between FeN₄ moiety and the graphene layer.

In addition, DFT calculations were performed to study the stability of these possible active site structures against demetallation under electrochemical environments. The proposed demetallation process of Fe is presented in **Supplementary Note 3**, **Supplementary Table 16**, and **Supplementary Figure 18**⁵⁶, which shows that Fe, together with adsorbed O₂, moves away from an N₄-coordinated state into an N₂-coordinated state. At the same time, the remaining two N atoms form N-H bonds with protons from the electrolyte. The Gibbs free energy for this demetallation process was predicted to be -0.02 eV for the S1 type FeN₄ site, lower than that of 0.26 eV for the S1-4H site (**Figure 6d**). This result indicates that the stability of the S1 site against

demetallation could be significantly improved by hydrogenating those carbon atoms immediately adjacent to a FeN₄ moiety, along with shortened Fe-N bonds caused by H₂ adsorption during the thermal activation.

In comparison, the S2-4H site shows a Gibbs free energy for the demetallation process of 1.31 eV, slightly higher than that of the S2 type FeN₄ site (1.27 eV), unveiling that the incorporation of hydrogen would enhance the stability of S2 site against demetallation just to a small degree. We predicted that the Fe-N bond length was 2.09 Å in S1-type FeN₄ and 2.05 Å in the S1-4H site, whereas the S2-4H site showed the same Fe-N bond length of 1.89 Å as the S2 site. This prediction is consistent with the reduction in R-values of the Fe-N bond in our XAS analysis of the Fe-N-C-FG catalyst. Further electronic structure analysis indicates that the bonding of H on C atoms in the S1-4H site could shift all the anti-bonding orbitals of central Fe above the Fermi energy level and thus lead to stronger Fe-N bonds with shortened length (Supplementary Note 4 and Supplementary Figures 19-20).

The intrinsic catalytic activity of S1(S2) and S1(S2)-4H FeN₄ sites following the 4e⁻ associative ORR pathway was investigated considering the solvation effect. The S1-4H showed insignificant change of limiting potential (*i.e.*, 0.01 V). In contrast, S2-4H sites increase the potential by 0.06 V than S2 site (**Figure 6c** and **Supplementary Figure 21**, and **Supplementary Note 5**). According to the Bader charge analysis, introducing surface H led to electron accumulation, thus weakening the adsorption of ORR intermediates and enhancing intrinsic activity of S2 sites.

As Fe NPs have been observed in the Fe-N-C-FG catalyst, DFT calculations were further performed to elucidate the role of Fe NPs encapsulated by graphene layers on the ORR activity of

the catalysts. According to Mössbauer spectroscopy and electron microscopy analyses, the Fe NP existed in the Fe-N-C-FG catalyst and was encapsulated in compact carbon shells (up to 14 layers). Here, we used the Fe(110) surface to model the extended facets of Fe NPs since (110) was predicted to be the energetically most favorable surface in body-centered cubic Fe⁵⁷. For simplification, only one layer of graphene was placed between a graphene layer containing a FeN₄ moiety and the Fe(110) surface (**Supplementary Figure 22**). We denoted this model as FeN₄-G-Fe (110) and predicted its limiting potential for ORR to be 0.68 V (**Figure 6f**). In comparison, we predicted the limiting potential for ORR on a FeN₄ site without a Fe surface underneath to be 0.66 V, indicating that the encapsulated Fe(110) surface had negligible impact on the ORR limiting potential of the FeN₄ site.

Conclusions

Current Fe-N-C catalysts still cannot provide comparable performance to replace Pt in hydrogen fuel cells. The primary limitations are insufficient metal site density and the challenging activity-stability trade-off involving active/unstable S1 and stable/less active S2 sites. In this work, we developed an effective approach to using an H₂/Ar forming gas for thermal activation, which significantly increases active metal site density with improved ratios of stable S2 sites, aiming to break the activity-stability trade-off.

The developed Fe-N-C catalyst exhibited exceptionally high activity in MEAs and generated 50.8 mA cm^{-2} at $0.9 \text{ V}_{iR\text{-free}}$ (1.0 bar O_2) and 191.0 mA cm^{-2} at 0.8 V (1.0 bar air), significantly exceeding DOE 2025 targets. The initial activity and performance are nearly comparable to a

typical Pt/C catalyst in aqueous acids and polymer electrolyte-based MEAs. Like the Pt/C catalyst, the Fe-N-C catalyst still degraded during the harsh ASTs. However, the significantly enhanced durability in MEAs was demonstrated to retain 67 mAcm⁻² at 0.8 V (air), which is encouraging and superior to other highly active Fe-N-C catalysts. Due to the intrinsic tolerance to methanol poisoning, the Fe-N-C cathode was studied in DMFCs, exhibiting a maximum power density of 275 mWcm⁻², substantially surpassing a Pt/C cathode (80 mWcm⁻²).

Extensive spectroscopic characterization and DFT calculations have been combined to elucidate the origin of improved activity and stability. We theoretically elucidated that the presence of H₂ facilitates the formation of S1 and S2-typed FeN₄ sites with significantly increased active site density. Hydrogenating those carbon atoms immediately adjacent to FeN₄ moieties during the thermal activation under forming gas leads to shortened Fe-N bonds, further experimentally verified using X-ray absorption spectroscopy. The shortened Fe-N bonds enhance intrinsic stability against demetallation during the ORR.

Meanwhile, based on extensive experimental characterizations, we suggested that these two different S1 and S2 sites may be located in different areas of carbon in catalysts. The intrinsically stable pyridinic N-coordinated FeN₄ sites (S2) may be embedded in the more graphitized double layers. In contrast, the less durable but more active pyrrolic N-coordinated FeN₄ sites (S1) are primarily hosted in less-graphitized and defective carbon surface planes. The proposed theory can well explain the promotional role of H₂ in suppressing S1 sites *via* the gasification of less stable carbon and retaining S2 sites in graphitized carbon in catalysts, thus leading to increased mesoporosity and enhanced stability.

Thus, compared to traditional inert atmosphere, optimal H₂ content during the thermal activation provides multiple benefits to simultaneously improve activity and stability of Fe-N-C catalysts, including (i) the increase of overall S1 and S2 site density, (ii) the increase of S2 to S1 ratios, (iii) shortened Fe-N bonds, (iv) hydrogenated Fe-N bonds with increased demetallation energy barrier, and (v) hydrogenated S2 sites with enhanced intrinsic activity. This work represents a critical step toward developing viable PGM-free catalysts with adequate performance and durability for PEMFCs.

Methods

Synthesis of Fe-N-C-n%FG. In a typical procedure, 10 mg Fe₂O₃ nanoparticles (Alfa-Aesar, 5 nm APS Powder) and 6.78 g zinc nitrate hexahydrate were dispersed and dissolved into a 150 mL methanol solution. The other 150 mL methanol solution contained 7.88 g 2-methylimidazole. Both solutions were mixed and heated at 60 °C for 24 hours. The precipitant was then collected by centrifuging, washed with ethanol three times, dried in a vacuum oven at 60 °C overnight, and finely ground to prepare the Fe₂O₃@ZIF-8 composite precursors. Next, the precursor was subject to be pyrolyzed at 1100 °C for one hour under forming gas (2-10 mol.% H₂ in Ar) to synthesize the Fe-N-C-n%FG catalysts. For comparison, the identical composite precursor was pyrolyzed at 1100 °C in Ar to synthesize the control sample, *i.e.*, Fe-N-C-Ar.

Morphology and Structure Characterizations.

⁵⁷Fe Mössbauer spectra were acquired at both room and low (6.5 K) temperatures and without applying an external magnetic field using a ⁵⁷Co/Rh source in constant acceleration modes. ⁵⁷Fe-

N-C catalysts were prepared with ⁵⁷Fe₂O₃ nanoparticles (⁵⁷Fe enrichment >95 %, American Elements) with the identical method mentioned above. The spectra were analyzed using the WinNormos program, a commercial package provided by WissEl–Wissenschaftliche Elektronik GmbH (Starnberg, Germany). Mössbauer doublets were fit using the Lorentzian mode of WinNormos.

Scanning electron microscopy images were obtained on a Focused Ion Beam-Scanning Electron Microscope (FIB-SEM, Carl Zeiss AURIGA CrossBeam). STEM imaging and EDS quantification were performed on an aberration-corrected JEOL NEOARM operated at either 60 or 80 kV in the Center for Nanophase Materials Sciences at Oak Ridge National Laboratory. Fe K-edge X-ray absorption spectroscopy was measured at beamline 11-2 at the Stanford Synchrotron Radiation Light source (SSRL). Data reduction, data analysis, and EXAFS fitting were performed with the Athena, Artemis, and IFEFFIT software packages.

Micromeritics TriStar II measured the N₂ isothermal adsorption/desorption for the catalysts at 77 K. The BET surface areas were derived with a correlation coefficient higher than 99.99 % and with positive constants. The distribution of porosity was determined with the classic cylinder model calculated by the DFT method (Halsey thickness curve). The micropore surface area was calculated by using *t*-Plot.

Electrochemical measurements.

An electrochemical workstation (CHI 760E) equipped with Pine AFMSRCE 3005 in a threeelectrode cell was employed to take all rotating disk electrode (RDE) measurements at room temperature in 0.5 M H₂SO₄ solution for all PGM-free catalysts. The Hg/Hg₂SO₄ (saturated K₂SO₄ electrolyte) electrode and a graphite rod were used as the reference and counter electrodes, respectively. A glassy carbon rotating-disk electrode (RDE) coated with the catalyst ink as the working electrode with a controlled loading of 0.6 mg cm⁻². The RDE was rotated at 900 r.p.m. for all measurements. During electrochemical measurements, the reference electrode was calibrated to a reversible hydrogen electrode (RHE) in the same electrolyte using a Pt black coated Pt wire with continuous H₂ bubble as the reversible hydrogen electrode. Steady-state polarization curves were recorded in O₂-saturated 0.5 M H₂SO₄ to determine the ORR activity using a potential staircase at a step of 0.05 V at an interval of 30 seconds from 1.0 to 0 V versus RHE. Four-electron selectivity and H₂O₂ yield during the ORR were determined by applying a high potential (1.10 V vs. RHE) on the ring electrode, leading to H₂O₂ electrooxidation during the ORR. An accelerated stress test (AST) was performed in O₂-saturated 0.5 M H₂SO₄ by potential cycling between 0.60 and 0.95 V_{RHE} at 50 mV s⁻¹. The CV profiles and ORR polarization plots were recorded after every 10,000 cycles to evaluate catalytic stability.

In-situ nitrite stripping for the determination of FeN_x site density (SD)

A catalyst loading of 0.20 mg cm⁻² was drop-casted onto a glassy carbon electrode (0.247 cm²) to carry out *in-situ* nitrite adsorption/stripping to determine active site density associated with atomically dispersed FeN₄ sites, due to the unique poisoning effect of nitrite on Fe. 0.5 M acetate buffer solution (pH 5.2) containing 125 mM NaNO₂ was employed as an electrolyte and prepared from sodium acetate (99.0 %) and glacial acetic acid. The active site density was determined. The

testing protocol developed by Kucernak et al.²⁸, including electrode cleaning, ORR performance measurement, poisoning, and stripping (recovery), was summarized in Supplementary Figure 23. It includes the following steps: (1) the working electrode was subjected to potential cycling between -0.4 and 1.0 V with a scan rate of 50 and 10 mV s⁻¹ in Ar-saturated electrolyte until a steady-state CV profile was obtained. (2) Evaluate the ORR activity of Fe-N-C catalysts (unpoisoned) in O₂-saturated electrolyte. Afterward, the baseline was recorded by cyclovoltammetry between -0.30 and 0.40 V in Ar-saturated electrolyte at a scan rate of 10 mV s⁻¹. (3) The working electrode was immersed in 125 mM NaNO₂ solution at open circuit potential for 5 minutes. The working electrode was then cleaned in deionized water (5 min), electrolyte (5 min) and deionized water (5 min) at a rotating rate of 300 r.p.m. (4) The ORR activity of the poisoned working electrode was measured in O₂-saturated electrolyte with the same parameters in Step 2. (5) The nitrite stripping was performed in an Ar-saturated electrolyte with identical parameters in Step (2). Step (2) was repeated to record the ORR activity after the recovery. Furthermore, a second nitrite poisoning was carried out on the recovered catalyst at the end, following the recent work by Kucernak et al., ²⁹ suggesting that the second nitrite adsorption/stripping is necessary to minimize any potential variation in the baseline CV profile due to the involvement of the ORR process. The site density was therefore calculated by using the second nitrite adsorption/stripping result.

The number of FeN_x active sites was quantified by the stripping charge of nitrite anions:

$$SD[sites \cdot g^{-1}] = \frac{Q_{\text{strip}}[C g^{-1}]N_{A}[atom \, mol^{-1}]}{n_{\text{strip}}F[C \, mol^{-1}]}$$
(1)

Where Q_{strip} is the coulometric charge associated with the stripping of nitrite; N_A is Avogadro's constant; n_{strip} (= 5) is the number of electrons associated with the reduction of one

adsorbed nitrite anion per site, F is Faraday's constant. The TOF (site⁻¹ s⁻¹, at 0.9 V) can be calculated from the kinetic current density i_k at 0.9 V and SD via:

TOF(@0.9 V versus RHE) [s⁻¹] =
$$\frac{i_k[A g^{-1}]N_A[mol^{-1}]}{SD[sites g^{-1}]F[A s mol^{-1}]}$$
 (2)

H₂-air fuel cell MEA tests. Both the anodes and cathodes were prepared using the catalyst-coated membrane (CCM) method using ultrasonic spray coating techniques. For the anode, the catalyst ink was prepared by mixing 20 wt.% Pt/XC-72 catalyst and ionomer dispersion (25wt. %, Aguivion D79-25BS) with an optimal ratio of ionomer to carbon (I/C) is 0.6. The solvent is a mixture of *n*-propanol and deionized water (DI-water) with 1:6 ratio. The prepared ink was firstly sonicated for 30 minutes in a water bath with a temperature under 30 °C followed by sonicating for 4 minutes using a sonic dismembrator (Fisher Scientific Model 120, Waltham, MA). The prepared ink was then sprayed onto a 5 cm² square Gore membrane by Exacta Coat spray machine (Sono-Tek, NY), and the Pt loading at the anode was controlled as 0.1 mg_{Pt}cm⁻². Cathode preparation was followed a similar protocol, but with a different n- propanol and DI-water ratio of 1:1. The prepared ink was sprayed on the opposite side of the anode, and the loading was controlled between 4.0-4.5 mg cm⁻². SGL-22BB gas diffusion layers were used to fabricate, which were measured by a fuel cell test station (Fuel Cell Technology, Inc., Albuquerque, NM, USA). First, the cell was heated to 80 °C with N₂ flow at 200 mL min⁻¹ in the anode and cathode for 2 hours, aiming to fully hydrate the membrane and ionomer. Then, air/oxygen flowing at 500 mL min⁻¹ and H₂ (purity 99.999 %) flowing at 300 mL min⁻¹ was supplied to the cathode and anode, respectively. The back pressures during the fuel cell tests were 150 kPa_{abs}. MEA performance under H₂-O₂ and

H₂-air conditions was measured by following the latest U.S. ElectroCat Consortium protocols.³³ Especially, the polarization curves were measured using the scan voltage method: in a range of 0.96 to 0.84 V at a scan rate of 20 mV per step holding 45 seconds. In a low voltage range of < 0.84 V, the scan rate is 40 mV per step for 45 seconds. MEA durability was evaluated by applying trapezoid potential on the cathode with following conditions: H₂/air (200 and 400 sccm), 100%RH, 150 kPa_{abs} back pressure, and 80 °C. The cathode was held at 0.95 V and 0.60 V each for 2.5 seconds. The ramping time from 0.60 to 0.95 V and back to 0.6 V is 0.25 seconds. A reference MEA with a Pt/C cathode (0.1 mg_{Pt} cm⁻²) was studied under identical AST conditions. MEA tests were performed in a differential cell with 14 parallel flow channels. The polarization curves were separately recorded at 5,000,10,000, 20,000, and 30,000 voltage cycles during the AST.³⁴

Direct methanol fuel cell tests. As for DMFC studies, while the Fe-N-C cathode is the same to hydrogen MEA, the anode catalyst ink was made from a PtRu/C (75 wt.%, JM). The anode ink was mixed PtRu/C catalyst with 2-propanol and 5 wt. % Nafion dispersion (D521) at an I/C ratio of 0.8 and a total PtRu loading of 3.0 mgcm⁻². Carbon fiber paper with a microporous layer (Sigracet 22BB) was used as anode GDL. A Nafion 212 membrane was used for MEA fabrication. The anode and cathode were purged with 1.0 M methanol aqueous solution and dry air at flow rates of 0.5 and 1000 sccm, respectively. The cell temperature was 94°C and the backpressure was 250 kPa_{abs}. The I-V polarization curves of the DMFC were recorded by scanning voltages from the OCV to 0.2 V with a staircase of 25 mV holding for 60 seconds. The MEA durability of DMFCs was evaluated by square wave AST, in which voltages were cycled between 0.40 and 0.80 V by

controlling a ramping time of 0.25 seconds and holding at each voltage for 2.5 seconds.

Computational methods. The first-principles DFT calculations^{58,59} were performed using the Vienna ab initio simulation package (VASP) code^{60,61}. The generalized gradient approximation (GGA) of Perdew, Burke, and Ernzernhof (PBE) functionals was used to describe the electronic exchange and correlation energy⁶². The energy cutoff was set as 400 eV to expand the wave function. The Brillouin zone was sampled using the Monkhorst-Pack 63 scheme with a 2 \times 3 \times 1 k-points grid for all modeled FeN₄ sites. A vacuum region of 14 Å thick was added in the direction normal to the carbon layer to ensure negligible interaction between the slab and its images. The optimized structures were obtained until the forces on each ion fell below 0.01 eV/Å. The computational hydrogen electrode method developed by Norskov et. al⁶⁴, was used to calculate the free energy change for the demetallation process. The aqueous environment of the electrolyte was treated with a continuum dielectric model as implemented by the Hennig group in the VASPsol code⁶⁵. The relative permittivity was set as 78.4 to model the water environment. Zero-point energy (ZPE) corrections were included in all the energies reported in this work. ZPE corrections were calculated as $ZPE = \frac{1}{2}\sum hv_i$, where h is Planck's constant and v_i is the frequency of the vibrational mode of binding molecules.

Data Availability

The authors declare that all data supporting the findings of this study are available within the paper and Supplementary Information files. Source data are provided with this paper.

Code Availability

All the DFT calculations were performed using the commercial software VASP. All the input and

output files of the calculations are available from Guofeng Wang per request.

Acknowledgement

We acknowledge the support from the U.S. Department of Energy (DOE), Energy Efficiency and Renewable Energy, Hydrogen and Fuel Cell Technologies Office. Scanning transmission electron microscopy research was supported by the Center for Nanophase Materials Sciences (CNMS), which is a US Department of Energy, Office of Science User Facility at Oak Ridge National Laboratory. This work was in part authored by Argonne National Laboratory, which is operated for the US DOE by the University of Chicago Argonne LLC under contract no. DE-AC02-06CH11357. G. Wu also thanks the New York State's Center of Excellence in Materials Informatics (CMI) at the University at Buffalo, and National Science Foundation (CBET-1604392, 1804326, and 2223467) for partial support.

Author Contributions Statement

G.W., J.P.D., and Y.Z. were the primary writers of the manuscript. Y.Z., J.L., B.Z., S.K. and G.W. designed catalyst synthesis and performed the electrochemical experiments, characterized the catalyst, and analyzed the data. C.L., and J. X. carried out fuel cell tests and data analysis. D.A.C., and M.J.Z. together performed the electron microscopy imaging and further characterizations. B.L., and G.F.W. designed and performed DFT calculations. M.L., M.W., and Z.F., designed and performed X-ray absorption spectroscopy and data analysis. R.P.H., E.E.A., B.L., and D.J.M. designed and performed Mössbauer spectroscopy experiments and data analysis. G.W. supervised the execution of the overall project.

Competing Interests Statement

The authors declare no competing interests.

Figure Captions

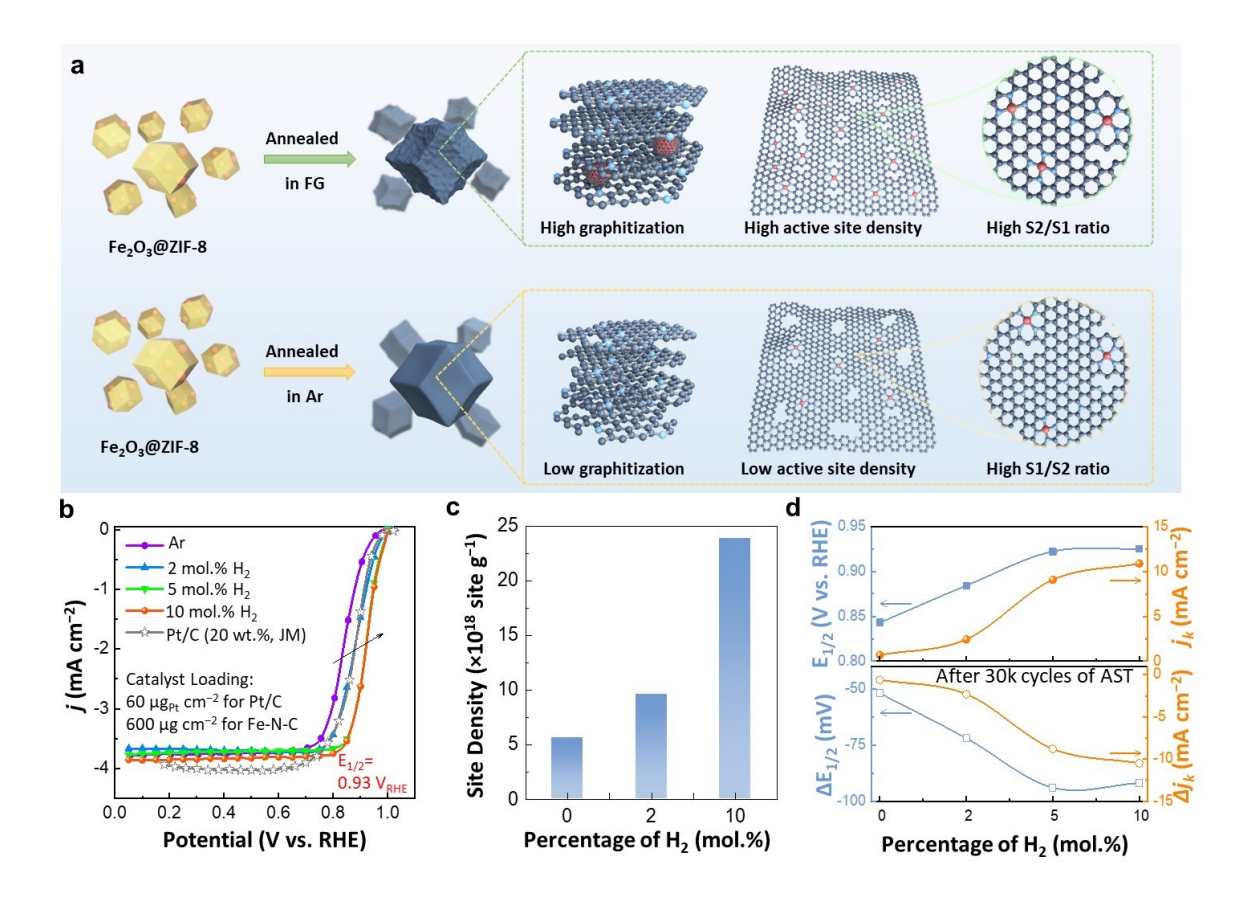


Figure 1. Synthesis principles and catalytic properties. (a) Schematic illustration of the construction of S1 and S2 sites *via* the control of the pyrolysis atmosphere. (b) Comparison of ORR activity of the Fe-N-C catalysts prepared in Ar and forming gas. A commercial Pt/C catalyst (60 μg_{Pt} cm⁻²) served as the baseline. The loadings for Fe-N-C catalysts are 0.6 mg cm⁻², the electrolyte is O₂-saturated 0.5 M H₂SO₄. (c) The changes of site density of the Fe-N-C catalysts prepared in the different atmospheres. (d) Evolution of activity and stability of Fe-N-C catalysts

prepared in the different atmospheres before and after 30,000 cycles of accelerated stress test.

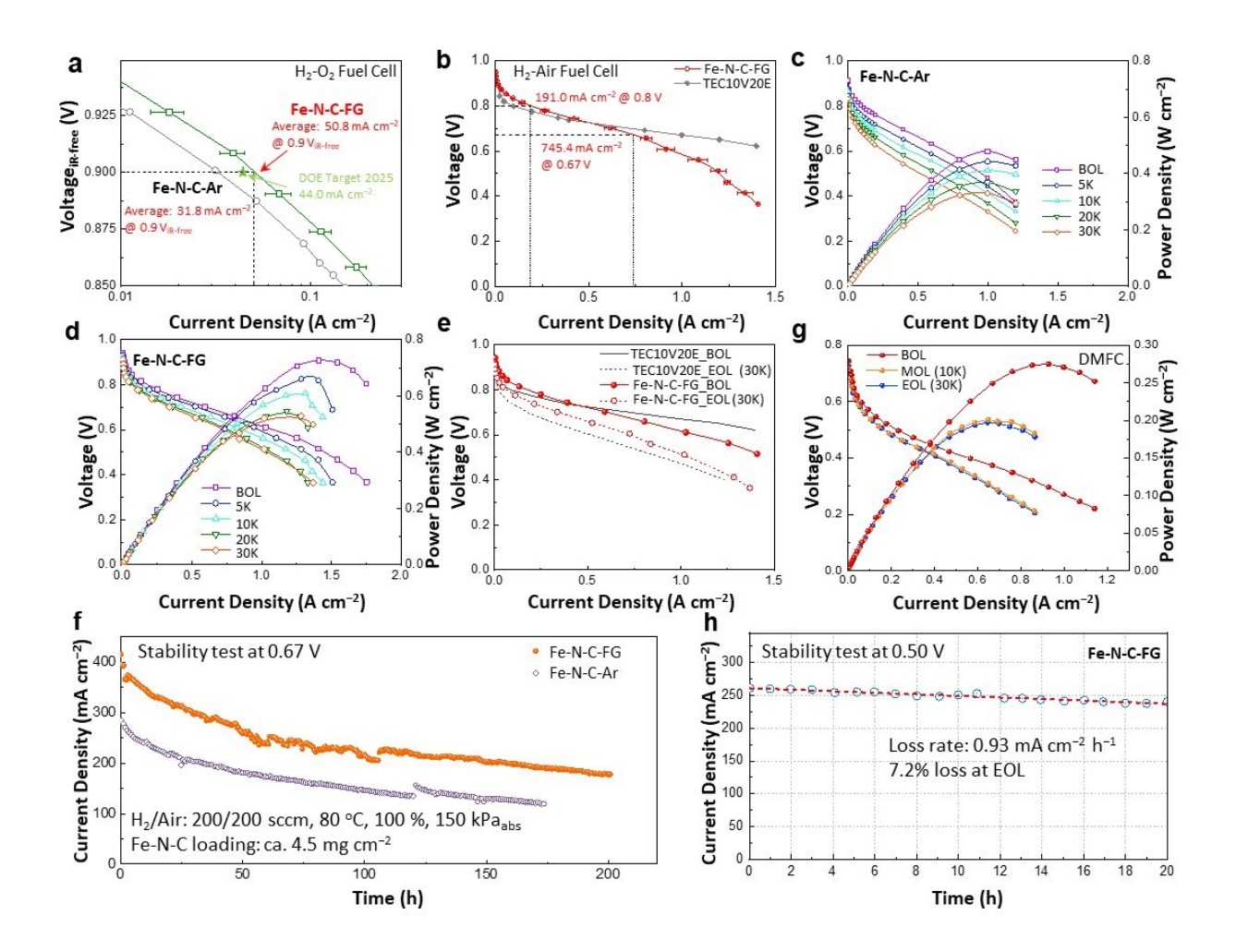


Figure 2. MEA performance of the Fe-N-C catalysts. (a) Determination of the catalysts' activities at 0.9 V_{iR-free} under 150 kPa_{abs} backpressure. The green star denotes the U.S. DOE target for 2025. (b) Comparison of H₂-air fuel cell performance of Fe-N-C-10%FG and a commercial Pt/C (0.1 mg Pt cm⁻²) cathode under 150 kPa_{abs} of air pressure and flow rates of 700/1700 sccm (H₂/air). H₂-air fuel cell performance of the Fe-N-C-Ar (c) and the Fe-N-C-FG catalyst (d) cathodes recorded at 75% RH during the 30,000 cycles of AST. (e) Comparison of I-V curves of the Fe-N-C-FG and Pt/C cathodes before and after 30,000 cycles of AST in H₂-air fuel cells. (f)

Long-term fuel cell life test under H₂-air conditions at a constant potential of 0.67 V (150 kPa_{abs} pressure and flow rates of air 200 sccm and H₂ 200 sccm). Direct methanol fuel cell (DMFC) performance of the Fe-N-C-FG cathode during the AST (g) and a short-term life test for 20 hours (h). The anode catalyst is 75% PtRu/C (JM) with a loading of 3.0 mg_{PtRu} cm⁻². The anode was purged with 1.0 M methanol solution with a flow rate of 0.5 sccm, the cathode was purged with dry air with a flow rate of 1000 sccm, the cell temperature was 94 °C, the back pressure in the cathode is 250 kPa_{abs}. Error bars stand for the standard deviation for three separate measurements.

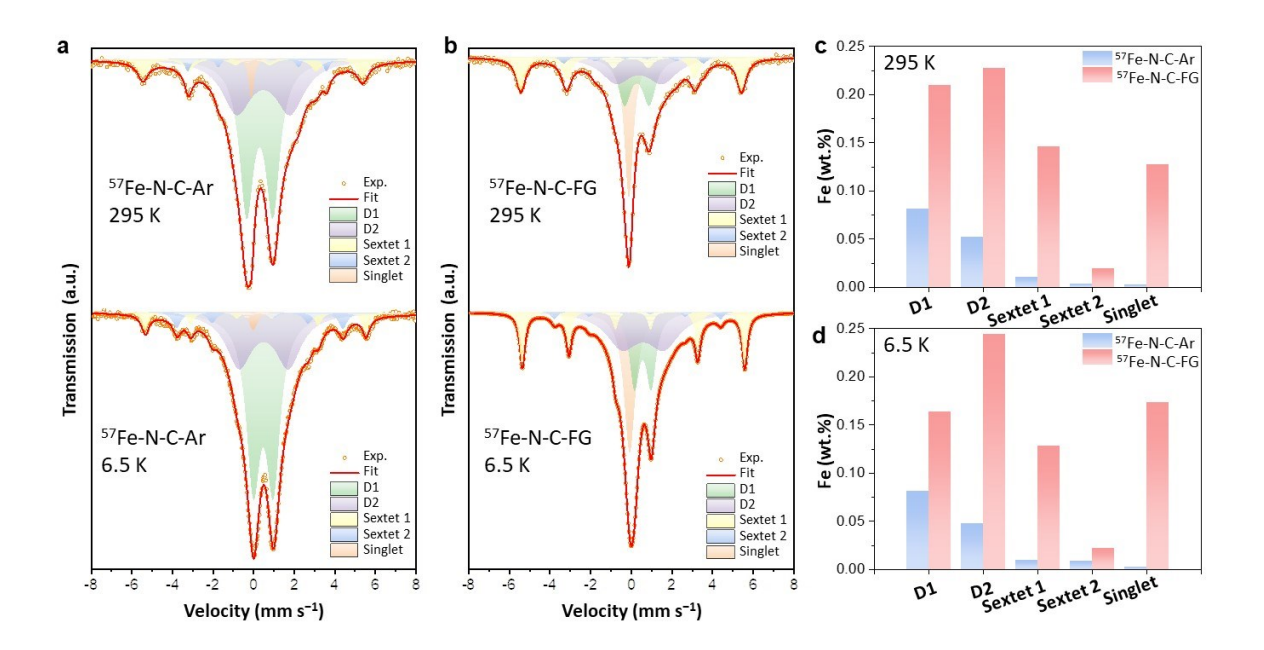


Figure 3. Analysis of Fe coordination environments induced from pyrolysis atmosphere. (a, b) The ⁵⁷Fe Mössbauer spectra of the Fe-N-C-Ar (a) and Fe-N-C-10%FG (b) catalysts at low and room temperature. (c, d) Comparison of D1, D2 and other components in the Fe-N-C-Ar and Fe-N-C-10%FG catalysts at room (c) and low (d) temperature.

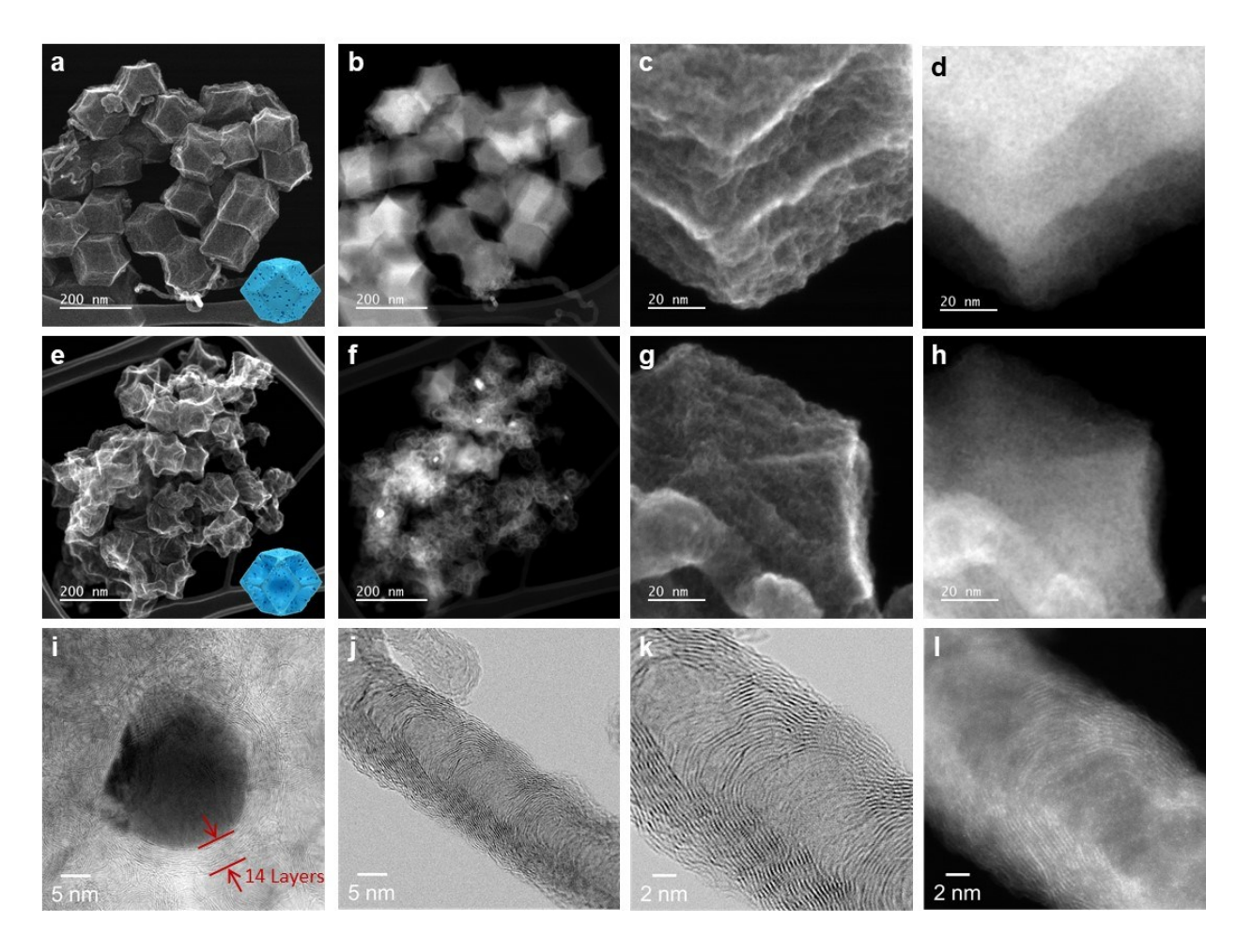


Figure 4. Morphologies of the Fe-N-C catalysts. (a and c) Secondary electron (SE) microscope images, and (d and e) high-angle annular dark-field scanning transmission electron microscope (HAADF-STEM) images of Fe-N-C-Ar. (e and g) SE microscope images, and (f and h) HAADF-STEM images Fe-N-C-FG. (i-k) BF-STEM images of Fe nanoparticles and multiwall carbon nanotubes in the Fe-N-C-FG, in which the Fe nanoparticle was encapsulated in the compact carbon shells. (l) HAADF-STEM image of multiwall carbon nanotube.

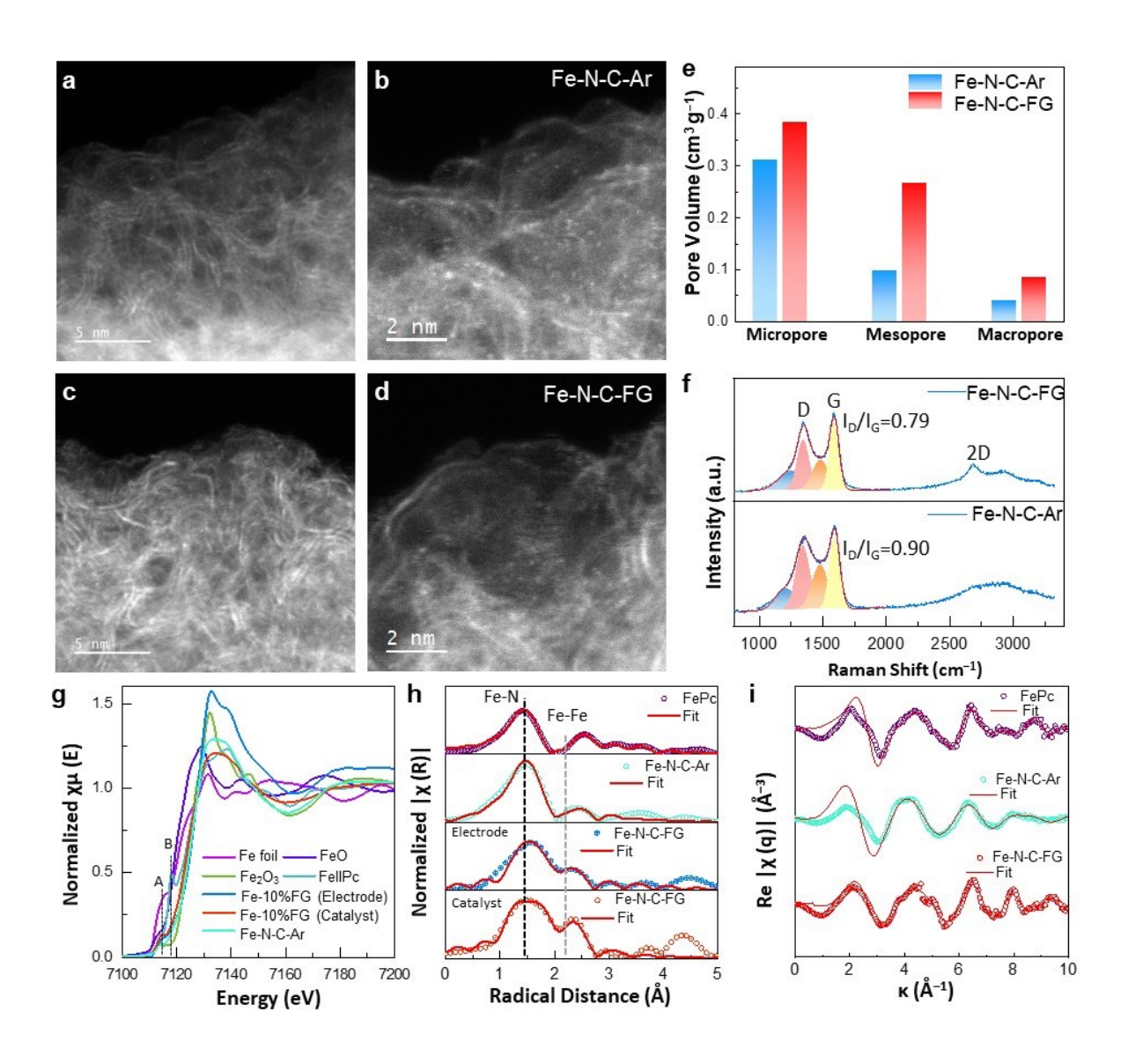


Figure 5. Structural analysis of the Fe-N-C catalysts. (a-d) ADF-STEM images of the Fe-N-C-Ar (a, b), and the Fe-N-C-FG (c, d). (e, f) Porosity distributions (e) and Raman spectra (f) of Fe-N-C-Ar and Fe-N-C-FG. (g-i) Fe K-edge XANES spectra (g) and Fourier-transformed EXAFS in R-space (h) and FT-EXAFS fitting curves in R spaces and q spaces (i) for Fe-N-C-Ar, Fe-N-C-FG and FePc.

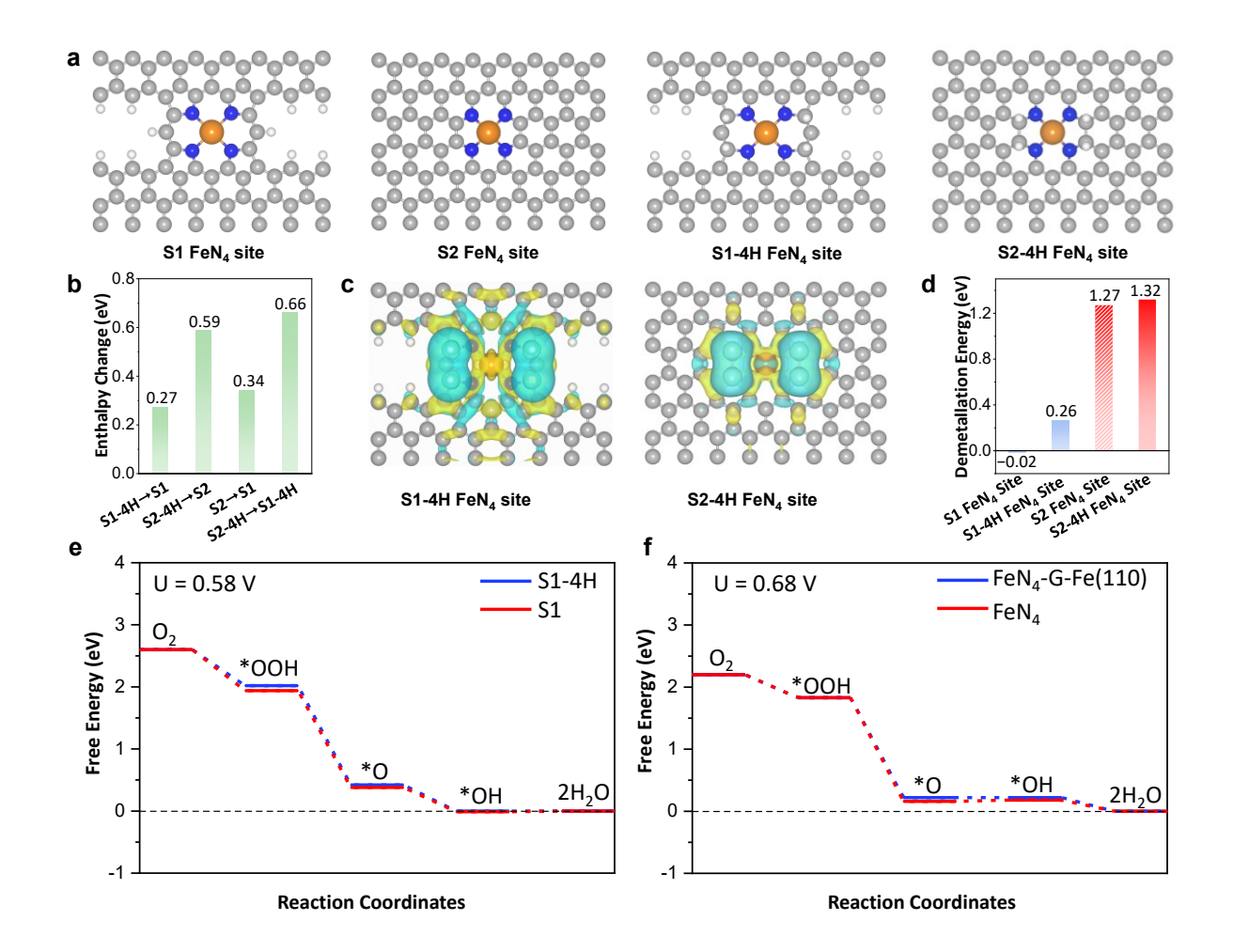


Figure 6. DFT calculations to elucidate the activity and stability improvement. (a) Atomistic structure of proposed S1 FeN₄ site, S2 FeN₄ site, S1-4H FeN₄ site, and S2-4H FeN₄ site. In this figure, the grey, blue, orange, and white balls represent C, N, Fe, and H atoms, respectively. (b) Comparison of the enthalpy changes for the transitions between S2 and S1, S1-4H and S1, S2-4H and S1-4H, and S2-4H and S2 FeN₄ site. (c) Charge density difference for the S1-4H and S2-4H site, which is calculated as $\rho(\text{FeN}_4+4\text{H *})-\rho(\text{FeN}_4)-\rho(4\text{H})$. Cyan and yellow represent charge accumulation and depletion in the region; the isosurface value is 0.002 e Å⁻³. (d) Comparison of the demetallation energies for S1-, S2-, S1-4H- and S2-4H-site. (e) Predicted free energy evolution for ORR through 4e⁻ associative pathway on S1- and S1-4H-site with solvation effect considered.

(f) Predicted free energy evolution for ORR through $4e^-$ associative pathway on FeN₄-G-Fe(110) site and FeN₄ site under electrode potentials of U = 0.68 V.

References

- Wang, X. X., Swihart, M. T. & Wu, G. Achievements, challenges and perspectives on cathode catalysts in proton exchange membrane fuel cells for transportation. *Nat. Catal.* **2**, 578-589 (2019).
- He, Y. & Wu, G. PGM-free oxygen-reduction catalyst development for proton-exchange membrane fuel cells: challenges, solutions, and promises. *Acc. Mater. Res.* **3**, 224-236 (2022).
- Wang, W., Jia, Q., Mukerjee, S. & Chen, S. Recent Insights into the Oxygen-Reduction Electrocatalysis of Fe/N/C Materials. *ACS Catal.* **9**, 10126-10141 (2019).
- 4 Martinez, U. *et al.* Progress in the Development of Fe-Based PGM-Free Electrocatalysts for the Oxygen Reduction Reaction. *Adv. Mater.* **31**, 1806545 (2019).
- Zhang, H. *et al.* Single Atomic Iron Catalysts for Oxygen Reduction in Acidic Media: Particle Size Control and Thermal Activation. *J. Am. Chem. Soc.* **139**, 14143-14149 (2017).
- 6 Liu, S. *et al.* Atomically-dispersed iron sites with a nitrogen-carbon coating as highly active and durable oxygen reduction catalysts for fuel cells. *Nat. Energy* **7**, 652-663 (2022).
- Asset, T., Maillard, F. & Jaouen, F. in *Supported Metal Single Atom Catalysis* (eds Philippe Serp & Doan Pham Minh) 531-582 (2022).
- 8 Glibin, V. P., Dodelet, J.-P. & Zhang, G. Energetics and thermodynamic stability of

- potential Fe(II)-hexa-aza-active sites for O₂ reduction in PEM fuel cells. *SusMat* **2**, 731-748 (2022).
- 9 Liu, S., Shi, Q. & Wu, G. Solving the activity–stability trade-off riddle. *Nat. Catal.* **4**, 6-7 (2021).
- Liu, K., Wu, G. & Wang, G. Role of Local Carbon Structure Surrounding FeN4 Sites in Boosting the Catalytic Activity for Oxygen Reduction. *J. Phys. Chem. C* **121**, 11319-11324 (2017).
- Mao, K., Yang, L., Wang, X., Wu, Q. & Hu, Z. Identifying Iron-Nitrogen/Carbon Active Structures for Oxygen Reduction Reaction under the Effect of Electrode Potential. *J. Phys. Chem. Lett.* **11**, 2896-2901 (2020).
- Shao, Y., Dodelet, J.-P., Wu, G. & Zelenay, P. PGM-Free Cathode Catalysts for PEM Fuel Cells: A Mini-Review on Stability Challenges. *Adv. Mater.* **31**, 1807615 (2019).
- Kumar, K. *et al.* On the influence of oxygen on the degradation of Fe-N-C catalysts. *Angew. Chem. Int. Ed.* **59**, 3235-3243 (2020).
- Zhu, Y. et al. Engineering Local Coordination Environments of Atomically Dispersed and Heteroatom-Coordinated Single Metal Site Electrocatalysts for Clean Energy-Conversion.
 Adv. Energy Mater. 10, 1902844 (2020).
- Li, J. *et al.* Identification of durable and non-durable FeN x sites in Fe–N–C materials for proton exchange membrane fuel cells. *Nat. Catal.* **4**, 10-19 (2021).
- Marshall-Roth, T. *et al.* A pyridinic Fe-N4 macrocycle models the active sites in Fe/N-doped carbon electrocatalysts. *Nat. Commun.* **11**, 5283-5297 (2020).

- Menga, D. *et al.* Resolving the Dilemma of Fe–N–C Catalysts by the Selective Synthesis of Tetrapyrrolic Active Sites via an Imprinting Strategy. *J. Am. Chem. Soc.* **143**, 18010-18019 (2021).
- Muñoz-Becerra, K., Venegas, R., Duque, L., Zagal, J. H. & Recio, F. J. Recent advances of Fe–N–C pyrolyzed catalysts for the oxygen reduction reaction. *Curr. Opin. Electrochem.* **23**, 154-161 (2020).
- Lefèvre, M., Dodelet, J. P. & Bertrand, P. O₂ Reduction in PEM Fuel Cells: Activity and Active Site Structural Information for Catalysts Obtained by the Pyrolysis at High Temperature of Fe Precursors. *J. Phys. Chem. B* **104**, 11238-11247 (2000).
- Wu, G., More, K. L., Johnston, C. M. & Zelenay, P. High-Performance Electrocatalysts for Oxygen Reduction Derived from Polyaniline, Iron, and Cobalt. *Science* **332**, 443-447 (2011).
- Proietti, E. *et al.* Iron-based cathode catalyst with enhanced power density in polymer electrolyte membrane fuel cells. *Nat. Commun.* **2**, 416-425 (2011).
- Lefèvre, M., Proietti, E., Jaouen, F. & Dodelet, J.-P. Iron-Based Catalysts with Improved Oxygen Reduction Activity in Polymer Electrolyte Fuel Cells. *Science* **324**, 71-74 (2009).
- Kramm, U. I. *et al.* On an Easy Way To Prepare Metal–Nitrogen Doped Carbon with Exclusive Presence of MeN4-type Sites Active for the ORR. *J. Am. Chem. Soc.* **138**, 635-640 (2016).
- Jaouen, F. & Dodelet, J.-P. O₂ Reduction Mechanism on Non-Noble Metal Catalysts for PEM Fuel Cells. Part I: Experimental Rates of O₂ Electroreduction, H₂O₂ Electroreduction,

- and H₂O₂ Disproportionation. J. Phys. Chem. C 113, 15422-15432 (2009).
- Tabassum, H. *et al.* Hydrogen generation via ammonia decomposition on highly efficient and stable Ru-free catalysts: approaching complete conversion at 450 °C. *Energy Environ*. *Sci.* **15**, 4190-4200 (2022).
- Kumar, K. *et al.* Fe–N–C Electrocatalysts' Durability: Effects of Single Atoms' Mobility and Clustering. *ACS Catal.* **11**, 484-494 (2021).
- Workman, M. J., Serov, A., Tsui, L.-k., Atanassov, P. & Artyushkova, K. Fe-N-C Catalyst Graphitic Layer Structure and Fuel Cell Performance. *ACS Energy Lett.* **2**, 1489-1493 (2017).
- Malko, D., Kucernak, A. & Lopes, T. In situ electrochemical quantification of active sites in Fe-N/C non-precious metal catalysts. *Nat. Commun.* 7, 13285-13292 (2016).
- Mehmood, A. *et al.* High loading of single atomic iron sites in Fe–NC oxygen reduction catalysts for proton exchange membrane fuel cells. *Nat. Catal.* **5**, 311-323 (2022).
- Zhang, H. *et al.* High-performance fuel cell cathodes exclusively containing atomically dispersed iron active sites. *Energy Environ. Sci.* **12**, 2548-2558 (2019).
- Zhang, H. *et al.* Single atomic iron catalysts for oxygen reduction in acidic media: particle size control and thermal activation. *J. Am. Chem. Soc.* **139**, 14143-14149 (2017).
- Laviron, E. Surface linear potential sweep voltammetry: Equation of the peaks for a reversible reaction when interactions between the adsorbed molecules are taken into account. *J. Electroanal. Chem. Interf. Electrochem.* **52**, 395-402 (1974).
- 33 Zhang, H. et al. Standardized protocols for evaluating platinum group metal-free oxygen

- reduction reaction electrocatalysts in polymer electrolyte fuel cells. *Nat. Catal.* **5**, 455-462 (2022).
- Osmieri, L., Cullen, D. A., Chung, H. T., Ahluwalia, R. K. & Neyerlin, K. C. Durability evaluation of a Fe–N–C catalyst in polymer electrolyte fuel cell environment via accelerated stress tests. *Nano Energy* **78**, 105209 (2020).
- Qiao, Z. et al. Atomically dispersed single iron sites for promoting Pt and Pt₃Co fuel cell catalysts: performance and durability improvements. *Energy Environ. Sci.* **14**, 4948-4960 (2021).
- Shi, Q. et al. Methanol tolerance of atomically dispersed single metal site catalysts: mechanistic understanding and high-performance direct methanol fuel cells. *Energy Environ. Sci.* 13, 3544-3555 (2020).
- Zitolo, A. *et al.* Identification of catalytic sites for oxygen reduction in iron- and nitrogendoped graphene materials. *Nat. Mater.* **14**, 937-942 (2015).
- 38 Kramm, U. I., Ni, L. & Wagner, S. ⁵⁷Fe Mössbauer Spectroscopy Characterization of Electrocatalysts. *Adv. Mater.* **31**, 1805623 (2019).
- Ni, L. *et al.* Identification of the Catalytically Dominant Iron Environment in Iron- and Nitrogen-Doped Carbon Catalysts for the Oxygen Reduction Reaction. *J. Am. Chem. Soc.* **144**, 16827-16840 (2022).
- Mineva, T. *et al.* Understanding Active Sites in Pyrolyzed Fe–N–C Catalysts for Fuel Cell Cathodes by Bridging Density Functional Theory Calculations and ⁵⁷Fe Mössbauer Spectroscopy. *ACS Catal.* **9**, 9359-9371 (2019).

- Thompson, E., Danks, A. E., Bourgeois, L. & Schnepp, Z. Iron-catalyzed graphitization of biomass. *Green Chem.* **17**, 551-556 (2015).
- Wang, M. & Feng, Z. Pitfalls in X-ray absorption spectroscopy analysis and interpretation:

 A practical guide for general users. *Curr. Opin. Electrochem.* **30**, 100803-100810 (2021).
- Mohd Adli, N. *et al.* Engineering Atomically Dispersed FeN4 Active Sites for CO₂ Electroreduction. *Angew. Chem. Int. Ed.* **60**, 1022-1032 (2021).
- Liu, S. *et al.* Chemical vapor deposition for atomically dispersed and nitrogen coordinated single metal site catalysts. *Angew. Chem. Int. Ed.* **59**, 21698-21705 (2020).
- Saveleva, V. A. *et al.* Fe–N–C Electrocatalyst and Its Electrode: Are We Talking about the Same Material? *ACS Appl. Energy Mater.* **6**, 611-616 (2023).
- Jaouen, F., Lefèvre, M., Dodelet, J.-P. & Cai, M. Heat-Treated Fe/N/C Catalysts for O₂ Electroreduction: Are Active Sites Hosted in Micropores? *J. Phys. Chem. B* **110**, 5553-5558 (2006).
- Zhao, X. *et al.* Single-Iron Site Catalysts with Self-Assembled Dual-size Architecture and Hierarchical Porosity for Proton-Exchange Membrane Fuel Cells. *Appl. Catal. B-Environ.* 279, 119400 (2020).
- Uddin, A. *et al.* High Power Density Platinum Group Metal-free Cathodes for Polymer Electrolyte Fuel Cells. *ACS Appl. Mater. Inter.* **12**, 2216-2224 (2020).
- Liu, Y. *et al.* Facile synthesis of MOF-derived concave cube nanocomposite by self-templated toward lightweight and wideband microwave absorption. *Carbon* **186**, 574-588 (2022).

- Zheng, L., Zhao, Y., Zhang, H., Xia, W. & Tang, J. Space-Confined Anchoring of Fe-Nx on Concave N-Doped Carbon Cubes for Catalyzing Oxygen Reduction. *ChemsusChem* **15**, e202102642 (2022).
- Ferrari, A. C. *et al.* Raman Spectrum of Graphene and Graphene Layers. *Phys. Rev. Lett.*97, 187401-187405 (2006).
- Wan, X. *et al.* Fe–N–C electrocatalyst with dense active sites and efficient mass transport for high-performance proton exchange membrane fuel cells. *Nat. Catal.* **2**, 259-268 (2019).
- Wu, G. & Zelenay, P. Nanostructured Nonprecious Metal Catalysts for Oxygen Reduction Reaction. *Acc. Chem. Res.* **46**, 1878-1889 (2013).
- 54 Hess, W. M. & Herd, C. R. in *Carbon Black* 89-173 (Routledge, 2018).
- Yu, M. & Trinkle, D. R. Accurate and efficient algorithm for Bader charge integration. *J. Chem. Phys.* **134**, 064111-064119 (2011).
- Xie, X. et al. Performance enhancement and degradation mechanism identification of a single-atom Co–N–C catalyst for proton exchange membrane fuel cells. *Nat. Catal.* 3, 1044-1054 (2020).
- Vitos, L., Ruban, A. V., Skriver, H. L. & Kollár, J. The surface energy of metals. Surf. Sci.411, 186-202 (1998).
- 58 Hohenberg, P. & Kohn, W. Inhomogeneous Electron Gas. *Phy. Rev. B* **136**, B864-B871 (1964).
- Kohn, W. & Sham, L. J. Self-Consistent Equations Including Exchange and Correlation Effects. *Phys. Rev.* **140**, 1133-1138 (1965).

- Kresse, G. & Furthmuller, J. Efficiency of ab-initio total energy calculations for metals and semiconductors using a plane-wave basis set. *Comput. Mater. Sci.* **6**, 15-50 (1996).
- Kresse, G. & Hafner, J. Ab initio molecular dynamics for liquid metals. *Phy. Rev. B* 47, 558-561 (1993).
- Perdew, J. P., Burke, K. & Ernzerhof, M. Generalized gradient approximation made simple.

 Phys. Rev. Lett. 77, 3865-3868 (1996).
- Monkhorst, H. J. & Pack, J. D. Special Points for Brillouin-Zone Integrations. *Phy. Rev. B* 13, 5188-5192 (1976).
- Norskov, J. K. *et al.* Origin of the overpotential for oxygen reduction at a fuel-cell cathode. *J. Phys. Chem. B* **108**, 17886-17892 (2004).
- Mathew, K., Sundararaman, R., Letchworth-Weaver, K., Arias, T. & Hennig, R. G. Implicit solvation model for density-functional study of nanocrystal surfaces and reaction pathways. *J. Chem. Phys.* **140**, 084106-084114 (2014).